



Molecular Physics

An International Journal at the Interface Between Chemistry and Physics

ISSN: 0026-8976 (Print) 1362-3028 (Online) Journal homepage: <https://www.tandfonline.com/loi/tmph20>

Cold temperatures invert product ratios in Penning ionisation reactions with argon

Natan Bibelnik, Sasha Gersten, Alon B Henson, Etay Lavert-Ofir, Yuval Shagam, Wojciech Skomorowski, Christiane P Koch & Edvardas Narevicius

To cite this article: Natan Bibelnik, Sasha Gersten, Alon B Henson, Etay Lavert-Ofir, Yuval Shagam, Wojciech Skomorowski, Christiane P Koch & Edvardas Narevicius (2019) Cold temperatures invert product ratios in Penning ionisation reactions with argon, *Molecular Physics*, 117:15-16, 2128-2137, DOI: [10.1080/00268976.2019.1594421](https://doi.org/10.1080/00268976.2019.1594421)

To link to this article: <https://doi.org/10.1080/00268976.2019.1594421>



Published online: 24 Mar 2019.



Submit your article to this journal [↗](#)



Article views: 110



View Crossmark data [↗](#)



Citing articles: 1 View citing articles [↗](#)

NIMROD MOISEYEV



Cold temperatures invert product ratios in Penning ionisation reactions with argon

Natan Bibelnik ^a, Sasha Gersten^a, Alon B Henson^a, Etay Lavert-Ofir^a, Yuval Shagam^{a*},
Wojciech Skomorowski ^{b**}, Christiane P Koch^b and Edvardas Narevicius^a

^aDepartment of Chemical and Biological Physics, Weizmann Institute of Science, Rehovot, Israel; ^bTheoretische Physik, Universität Kassel, Kassel, Germany

ABSTRACT

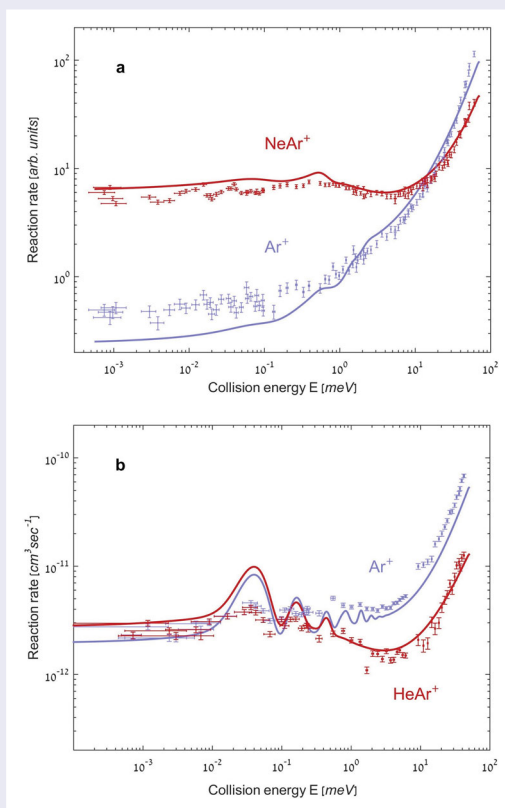
In many chemical reactions with more than one possible outcome, the branching ratio, which is the ratio between the different reaction paths, is nearly constant over a wide range of collision energies. In barrierless systems governed by long-range interactions, however, the branching ratio is more sensitive to collision energy, and its dependence on it can be useful for better understanding the dynamics and reconstructing interaction potentials. Here we present the reaction rates of Penning and associative ionisation of metastable neon and helium with argon atoms. We obtain reaction rates in merge beam experiments, over a wide range of collision energies corresponding to that of room temperature, all the way down to a few millikelvins. We observe a change of two orders of magnitude in the branching ratio in the measured collision energy range and explain these changes using theoretical calculations.

ARTICLE HISTORY

Received 31 July 2018
Accepted 6 March 2019

KEYWORDS

Branching ratio; Cold collisions; Merged beam; Penning ionisation; Associative ionisation



CONTACT Edvardas Narevicius  edvardas.narevicius@weizmann.ac.il  Department of Chemical and Biological Physics, Weizmann Institute of Science, Rehovot 76100, Israel

*Present address: JILA, NIST and the University of Colorado, Department of Physics, University of Colorado, Boulder, Colorado 80309–0440, USA

**Present address: Department of Chemistry, University of Southern California, Los Angeles, California 90089, USA

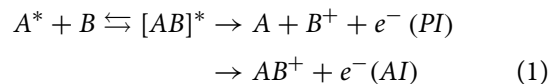
Introduction

One of the central goals of the chemical sciences is to obtain a comprehensive characterisation and microscopic understanding of chemical processes. An important parameter in describing a chemical reaction with more than one possible outcome is the branching ratio. Very often, it is determined empirically and is assumed to vary slowly with changes in the collision energy. Nevertheless, the dependence of the branching ratio on the collision kinetic energy reveals interesting information about the reaction dynamics. In order to observe significant changes in the branching ratio, it is essential to perform measurements over a wide range of collision energies. In our experiments, we measure the branching ratio over collision energies ranging from room temperature, where classical models can explain the dynamics, down to the cold collision regime, where the reaction dynamics is largely governed by quantum effects.

Due to centrifugal repulsion between the chemical reactants, at sufficiently low kinetic energies, only a few angular momentum states or partial waves contribute to the reaction dynamics. This typically occurs below 1 K, for weakly interacting molecules, where both the exact position and height of the centrifugal barrier depend on the interaction strength and the reduced mass. The effect enables the observation of interesting quantum phenomena that are highly sensitive to the interaction details and can be used as benchmarks for reconstructing potential energy surfaces.

In recent studies, cold collision experiments have been conducted using several techniques. Hybrid ion-neutral traps have been used to investigate ion-neutral interactions in systems involving neutral species (such as Rb, Ca, and Yb), confined in magneto-optical traps, and ionic species (such as laser-cooled Yb^+ and Ca^+ , sympathetically cooled N_2^+ and buffer gas-cooled OH^-), confined in Paul traps [1–4]. In other experiments, cold effusive beams have been implemented in studying the interactions of H, He, H_2 , and D_2 , with buffer gas-cooled CH_5^+ and H_3^+ ions [5]. In all these ion-neutral experiments, there was no significant change in the branching ratio throughout the measured collision energy range. A convenient method for studying cold neutral-neutral interactions is via merged beam experiments, which offer a unique possibility to probe the reaction dynamics over a wide energy range, from hundreds of kelvins down to several millikelvins [6,7]. Currently, merged beam studies focus on chemionization processes, where neutral species interact with electronically excited noble gas atoms via van der Waals dispersion forces [8–13]. Possible reaction channels include Penning ionisation (PI) [14,15], where the neutral reactant is ionised, whereas the excited reactant is quenched, associative ionisation (AI), where a

molecular ion is formed, or dissociative ionisation (DI), where a reactant molecule breaks down into ionic and neutral fragments. Our experiments focus on AI and PI processes, which are described by:



The branching ratio between PI and DI channels has been probed in systems characterised by strong short-range interactions, such as Ne^* with NH_3 , ND_3 , and CH_3F . It was found to be constant over the collision energy range of 230 K to 100 mK in ammonia isotopes [12], and of 56 K to 150 mK in fluoromethane [13]. The weak dependence on collision energy in these systems can be explained by comparing the interaction strength with the initial kinetic energy of the reactants; the short-range chemical rearrangement is fully governed by the deep potential well; the initial kinetic energy has a negligible effect on the reaction dynamics.

Here, we demonstrate that for weakly interacting systems where the interaction strength is of the order of the collision energy, strong changes in the branching ratio can be expected over a wide energy range. Importantly, we show that the AI to PI branching ratio for the $\text{Ne}(3^3\text{P}_2) + \text{Ar}$ reaction changes by more than two orders of magnitude over collision energies corresponding to room temperature down to several millikelvins. At the highest collision energies, Ar^+ is the major product, whereas at the lowest collision energies, the formation of the molecular ion, NeAr^+ , is the dominant channel. A similar trend is observed in the $\text{He}(2^3\text{S}_1) + \text{Ar}$ reaction, with a roughly equal tendency towards the AI and PI channels at the lowest collision energies. Our theoretical calculations for the branching ratio and the reaction rates are in agreement with the experimental results. The theoretical calculations also show that PI processes that take place at large inter-nuclear distances are especially sensitive to the long-range part of the product's ion-neutral interaction and this explains the difference in the branching ratio between $\text{Ne}^* + \text{Ar}$ and $\text{He}^* + \text{Ar}$ at low collision energies.

Experimental methods

Our experimental setup is based on a magnetically aligned merged beam apparatus, where controlled collisions between two species, of which one is paramagnetic, can be studied. This setup has been described in detail previously [7,9,11].

In our experiment, we generate a supersonic beam of metastable species, $\text{He}(3^3\text{S}_1)$ or $\text{Ne}(3^3\text{P}_2)$ by applying a dielectric barrier discharge [16] on ground-state He or Ne, respectively, at the orifice of an Even-Lavie pulsed

valve [17]. We then use a magnetic guide to deflect the low-field seeking fraction of the metastable beam, and merge it with a straight Ar beam, which is generated by a second pulsed valve. The two beams collide in a detection region of a pulsed time-of-flight mass spectrometer, which distinguishes the different ionic products by their mass-to-charge ratio. We use a multi-channel plate detector, which is placed on axis with the beam, for measuring the metastable reactants, and an electron impact ionisation time-of-flight mass spectrometer for detecting the neutral argon atoms from the straight beam.

The collision energy range is obtained by tuning the relative velocity between the beams. This is achieved by modifying the stagnation temperatures of the valves and by seeding the Ar beam in carrier gases having different masses (such as He or H₂). In addition to the narrow velocity spread created in the supersonic expansion, the attainable energy spread is further reduced by two orders of magnitude due to velocity-position space correlations that develop during the free propagation of the pulsed beams [18]. The current configuration allows one to measure PI and AI reaction rates as a function of collision energy spanning from ten millikelvins to hundreds of kelvins.

Theoretical methods

In order to calculate PI and AI cross sections and reaction rates, we combine two methods. We use discrete variable representation (DVR) [19] for calculating the branching ratio between bound (AI) and continuum states (PI) at the exit channel, and phase-shift calculations for computing the total ionisation cross section. Ideally, DVR should enable the calculation of the cross section for every exit channel. However, it is based on matrix diagonalization; therefore, the attainable number of the calculated states at low energies is insufficient for obtaining the full spectrum in detail. Nevertheless, it is enough for obtaining the branching ratio, which is a smooth function of the collision energy.

PI and AI can be described as auto-ionisation processes of a particle with reduced mass, μ , in an effective potential that depends only on the inter-nuclear coordinate, R , and on the angular momentum of the collision, l . We assume that the transition is irreversible and therefore can be represented by an optical potential $-\frac{i}{2}\Gamma(R)$, where $\Gamma(R)/\hbar$ is the decay rate. The entrance Hamiltonian is given by:

$$H_i(R) = \hat{T} + \frac{\hbar^2 l(l+1)}{2\mu R^2} + V_{\text{reactants}}(R) - \frac{i}{2}\Gamma(R), \quad (2)$$

where \hat{T} is the radial kinetic energy operator.

The total ionisation cross section for reactants with partial wave l and collision energy E_i is given by the formula:

$$\sigma_{\text{total}}^l(E_i) = (2l+1) \frac{\pi}{k^2} (1 - e^{-4\text{Im}(\delta_l)}), \quad (3)$$

where $k = \sqrt{2\mu E_i}$ and δ_l represents the complex phase shift, which is computed using Johnson's integration method [20].

We obtain the ionic product wave functions as eigenstates of the Hermitian Hamiltonian:

$$H_f(R) = \hat{T} + \frac{\hbar^2 l(l+1)}{2\mu R^2} + V_{\text{products}}(R). \quad (4)$$

In order to distinguish the contributions of the different exit channels to the total ionisation cross section, we use the following approximate expression suggested by Hickman and Morgner [21]:

$$\sigma_{\text{total}}^l(E_i) = \int_{E_f} \frac{4\pi}{k^2} \left(\frac{2\mu}{\hbar^2} \right)^2 \left(\frac{1}{2\pi} \right) (2l+1) e^{-2\text{Im}(\delta_i)} \left| \langle \psi_f^l | \sqrt{\Gamma} | \psi_i^l \rangle \right|^2 dE_f, \quad (5)$$

where ψ_i^l is the initial reactant eigenstate with energy E_i , ψ_f^l are the final product eigenstates with energy E_f , and Γ is the ionisation width. Note that the matrix elements, $\left| \langle \psi_f^l | \sqrt{\Gamma} | \psi_i^l \rangle \right|^2$, represent the overlap of the states ψ_f^l with the reactive fraction of the incoming wave function $\sqrt{\Gamma} | \psi_i^l \rangle$.

The relative contribution of the AI process to the total ionisation cross section is given by the ratio of the contributions of all final bound states ($E_f < 0$) versus that of all possible final states:

$$\frac{\sigma_{\text{AI}}^l(E_i)}{\sigma_{\text{total}}^l(E_i)} = \frac{\sum_{E_f < 0} \left| \langle \psi_f^l | \sqrt{\Gamma} | \psi_i^l \rangle \right|^2}{\sum_{\text{all } E_f} \left| \langle \psi_f^l | \sqrt{\Gamma} | \psi_i^l \rangle \right|^2}. \quad (6)$$

We use DVR [19] to calculate the eigenstates, ψ_i^l and ψ_f^l , with eigen-energies E_i and E_f , from the reactant and product Hamiltonians. In the above expression, we sum up the bound states and integrate over the continuum part of the spectrum. We perform the calculation separately for every angular momentum l , and obtain a different set of eigen-energies for each partial wave. Therefore, we have to interpolate over a common energy grid before summing the contributions of all the partial waves. The DVR calculated ratio, $\sigma_{\text{AI}}^l / \sigma_{\text{total}}^l$, is a smooth function of the collision energy. We interpolate the ratio of every partial wave over the common energy grid, and multiply it by the cross section, σ_{total}^l , which we compute using phase shift calculations.

We sum over all angular momenta and obtain the total AI and PI cross sections:

$$\sigma_{AI}(E) = \frac{\pi}{k^2} \sum_l (2l+1) \left(1 - e^{-4\text{Im}(\delta_l)}\right) \frac{\sigma_{AI}^l}{\sigma_{total}^l}(E) \quad (7)$$

$$\sigma_{PI} = \sigma_{total} - \sigma_{AI}. \quad (8)$$

We multiply σ by $\hbar k/\mu$ to obtain the reaction rates.

For simplicity, we neglect the angular momentum carried by the electron. This assumption is supported by a semi-classical calculation that limits the angular momentum transfer to two quanta for He + Ar, and one quantum for Ne + Ar, at low transfer probabilities. To further validate the assumption, we have included the angular momentum transfer to the electron in a few test calculations [22] (without optimising all

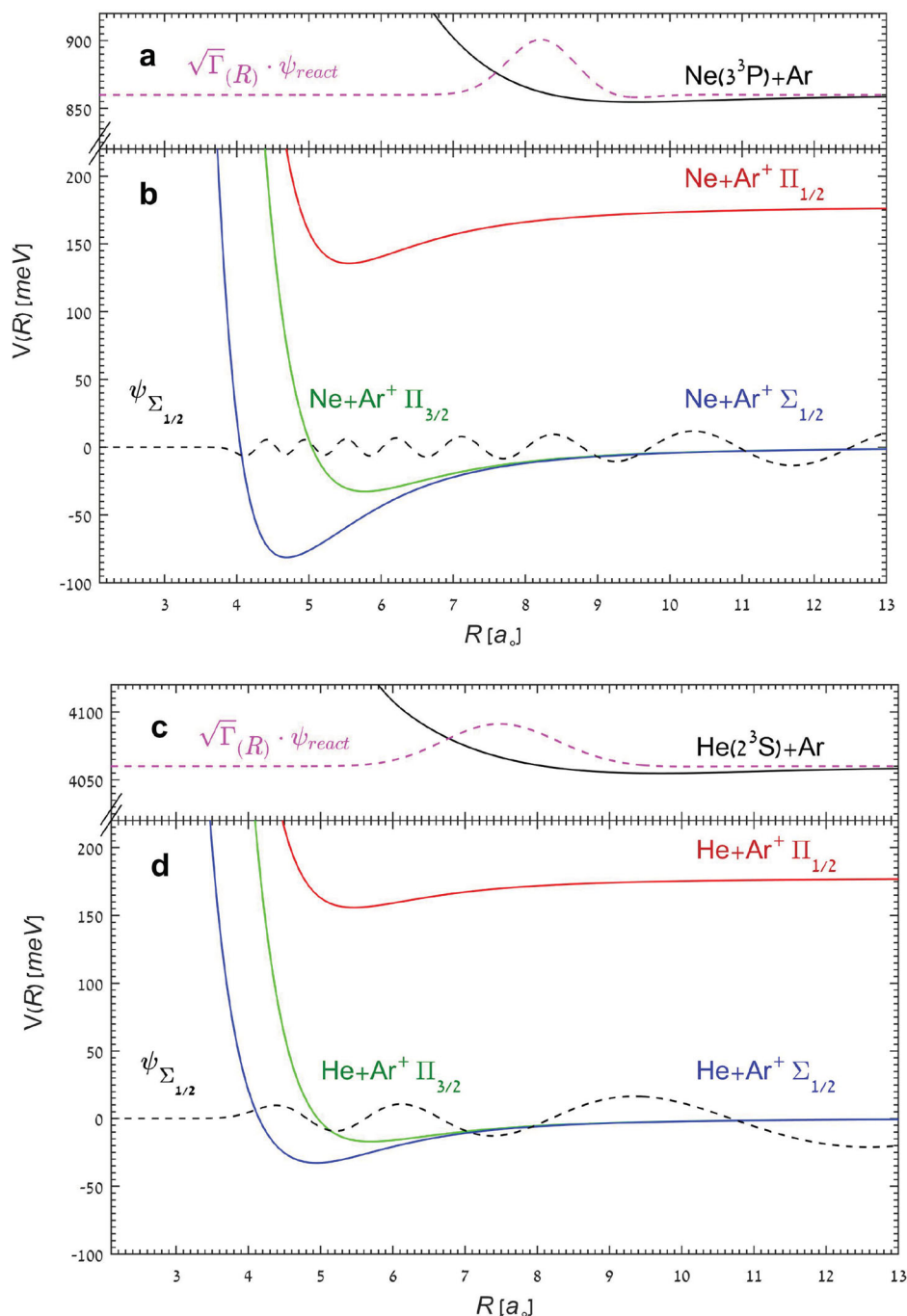


Figure 1. The neutral and ionic potential energy surfaces for Ne(3^3P) + Ar (a and b) and He(2^3S) + Ar (c and d). The incoming wave function weighted by the reaction rate $\sqrt{\Gamma}$ (dashed pink line, a and c), and the outgoing $\Sigma_{1/2}$ continuum wave function (dashed black line, b and d), both for angular momentum $l = 0$ and wave number $k = 8.10^9 \text{ m}^{-1}$, are presented for the two systems. In the Ne(3^3P) + Ar system (b), the continuum wave function oscillates faster and therefore the overlap with the weighted incoming wave function is smaller (colour online).

Table 1. Parameters for the neutral potential energy curves. The parameters ($A, \alpha, \beta_1, \beta_2$ in Siska et al.) are obtained by least squares fitting of the log difference between the calculated and measured AI and PI rates. [†] The decay rate pre-exponential factor A is estimated after calibration of the rates, which is based on previous measurements of the total $\text{He}^* + \text{Ar}$ ionisation cross sections [25].

Parameter	$\text{He}^* + \text{Ar}$		$\text{Ne}^* + \text{Ar}$	
	This work	Siska <i>et al.</i> [23]	This work	Gregor <i>et al.</i> [24]
β_1	5.45Å	5.523Å	6.53Å	5.978Å
β_2	7.04Å	7.108Å	5.88Å	5.333Å
α	$3.9 \pm 0.2 \text{Å}^{-1}$	3.889Å^{-1}	$4.8 \pm 0.2 \text{Å}^{-1}$	$1.472 \pm 0.2 \text{Å}^{-1}$
A^\dagger	$1.03 \cdot 10^4 \text{Kcal mole}^{-1}$	$2.07 \cdot 10^4 \text{Kcal mole}^{-1}$		

potential parameters). The rates obtained with and without angular momentum transfer turned out to be very similar.

In the numerical calculations, we use the neutral potential model of Siska [23,24], Figure 1(a and c), which is a Morse-spline-van der Waals-type potential with decay $\Gamma = Ae^{-\alpha R}$. We adjust the fitted parameters of the original paper ($A, \alpha, \beta_1, \beta_2$) to obtain the best fits to our experimental results, as presented in Table 1.

In the product channel, Figure 1(b and d), we use three spin-orbit-resolved ionic potentials of $\text{Ar}^+ + \text{He}$ or $\text{Ar}^+ + \text{Ne}$: $\Sigma_{1/2}$, $\Pi_{3/2}$ and $\Pi_{1/2}$ [26]. We obtain the non-relativistic $^2\Sigma$ and $^2\Pi$ interaction potentials for $\text{Ar}^+ + \text{He}$ or $\text{Ar}^+ + \text{Ne}$ from *ab initio* supermolecular calculations using a spin-unrestricted coupled cluster method with single, double, and noniterative triple excitations [UCCSD(T)], as implemented in the Molpro suite of codes [27]. We employ a correlation-consistent doubly augmented d-aug-cc-pVQZ basis set for the helium atom, and a singly augmented aug-cc-pVQZ basis set for the neon and argon atoms. We calculate the spin-orbit-coupled states, $\Sigma_{1/2}$, $\Pi_{1/2}$ and $\Pi_{3/2}$, assuming that constant spin-orbit coupling is equal to the asymptotic splitting in $\text{Ar}^+(^2P)$ ion.

We assume an equal probability of decay into each ionic final spin-orbit state. We also assume a full predissociation of $\text{HeAr}^+(\Pi_{1/2})$ to $\text{He} + \text{Ar}^+$ with an ultimate contribution only to the PI channel. This is justified by comparing the short lifetime of $\text{HeAr}^+(\Pi_{1/2})$ of less than a microsecond [26], to the detection duration of 12 microseconds.

Finally, we perform a convolution of the calculated rates with our supersonic beam profile, which has a velocity spread of 10 m/s.

Results

The measured PI and AI reaction rates in the two systems, $\text{Ne}(^3P) + \text{Ar}$ and $\text{He}(^3S) + \text{Ar}$, are presented in Figure 2. Interestingly, the systems exhibit a strong and very different dependence of the branching ratio as a function of the collision energy.

At high energies, the dominant channel is PI, with the Ar^+ ion product. At low collision energies, however, we observe a change in the trend, and a significant difference exists in the branching ratios between the two systems. Whereas in the $\text{Ne}^* + \text{Ar}$ reaction the molecular ion product, NeAr^+ , dominates over Ar^+ by an order of magnitude at collision energies below 0.1 meV, in the $\text{He}^* + \text{Ar}$ reaction, the branching ratio reaches unity.

Discussion

Our molecular dynamics calculations are in a good agreement with the experimental results, as shown in Figure 2. An intuitive explanation for the changes in the branching ratio can be given in terms of the overlap of the final bound (AI) and continuum (PI) ionic states, with the incoming wave function weighted by the square root of the reaction rate, $\sqrt{\Gamma} \cdot \psi_i$. In both explored systems, the calculations indicate strong modifications in the shape of $\sqrt{\Gamma} \cdot \psi_i$ when lowering the collision energy. This leads to different overlaps of $\sqrt{\Gamma} \cdot \psi_i$ with the bound and continuum final states and thus to a non-trivial dependence of the branching ratio on the collision energy. In contrast, in systems with strong short-range interactions, the reaction occurs at the short range, where the interaction strength is much larger than the collision energy. In such systems, $\sqrt{\Gamma} \cdot \psi_i$ is less sensitive to variations in the collision energy, the overlap with different final states exhibits a minor dependence on the collision energy, and the branching ratio is approximately constant over a large collision energy range. Figure 3 presents the calculated $\sqrt{\Gamma} \cdot \psi_i$ of two collision energies, for the $\text{Ne}(^3P_2) + \text{Ar}$ potential, and for the $\text{Ne}(^3P_2) + \text{Ar}$ potential scaled by a factor of ten. The presented collision energies, 0.1 and 10 meV, are respectively, smaller and larger than the potential well depth, of 5.4 meV. Both collision energies are smaller than the scaled potential well depth, of 54 meV. Whereas the overlap of the two $\sqrt{\Gamma} \cdot \psi$ with different energies of the $\text{Ne}(^3P_2) + \text{Ar}$ potential is 41%, the overlap of the two $\sqrt{\Gamma} \cdot \psi$ of the scaled potential is 86%. In the former case, the difference in the shape of $\sqrt{\Gamma} \cdot \psi$ leads to different overlaps with the final ionic states and

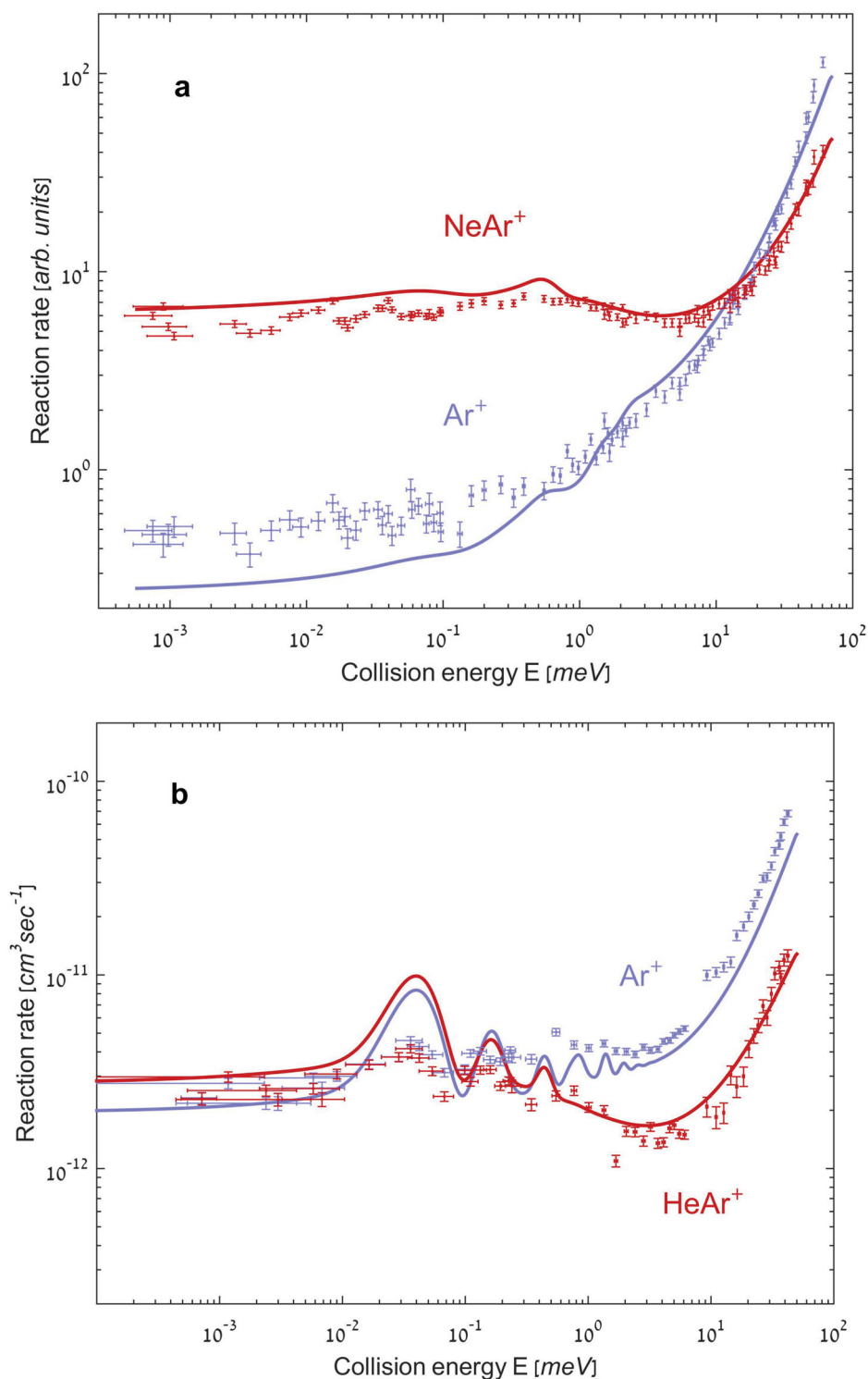


Figure 2. Associative ionisation (red) and Penning ionisation (blue) reaction rates of $\text{Ne}(^3\text{P}) + \text{Ar}$ (a) and $\text{He}(^3\text{S}) + \text{Ar}$ (b). The solid lines denote numerical simulations. The two resonances (b) at 0.04 meV and 0.16 meV match $l = 6$ and $l = 7$, respectively. In $\text{He}^* + \text{Ar}$, the reaction rate is calibrated to match previous measurements of the total ionisation cross section [25] (colour online).

therefore to a variation in the branching ratio, which is measured experimentally. In the latter case, however, where the collision energies are much smaller than the potential well depth, the change in the shape of the wave

functions is negligible and the branching ratio remains approximately constant.

Our model also explains the significant differences in branching ratios at low energies, between $\text{Ne}(^3\text{P}) + \text{Ar}$

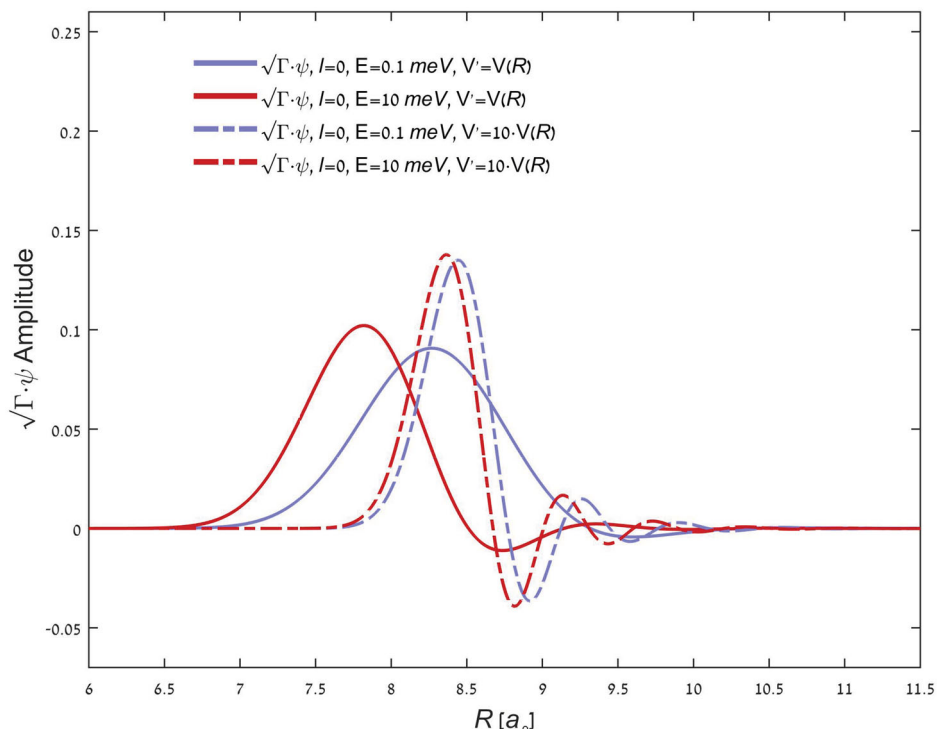


Figure 3. Incoming $l = 0$ wave functions weighted by $\sqrt{\Gamma}$ of the reactant potential $\text{Ne}(^3\text{P}) + \text{Ar}$ (solid lines) and of the reactant potential scaled by a factor of ten (dashed line) for collision energies smaller and larger than the potential depth well of $\text{Ne}^* + \text{Ar}$ potential (both are smaller than the scaled potential well depth). The weighted wave functions, $\sqrt{\Gamma} \cdot \psi$, are normalised, so that $\int |\psi_{(R)}|^2 \Gamma_{(R)} dR = 1$.

and $\text{He}(^3\text{S}) + \text{Ar}$, which share a similar neutral potential dominated by strong repulsion at the short range, together with weak long-range Van der Waals interactions. The weighted incoming wavefunction, $\sqrt{\Gamma} \cdot \psi_i$, contributes mainly in a region of the ionic potential that is dominated by the long-range C_4/R^4 ion-induced dipole interaction term, shown in Figure 1(b and d). In this region, the continuum wave functions (PI) are sensitive to the interaction strength, i.e. the potential well depth of the exit channel. Stronger interactions lead to faster oscillations of the outgoing continuum wave functions and thus to a smaller overlap with the weighted incoming wave function. This consequently leads to a smaller PI rate; however, the effect on the bound states (AI) is minor. This results in an increased AI/PI branching ratio at low energies. On the other hand, at high energies, the PI channel is always preferred, since partial waves of higher angular momentum, which lack bound states, become accessible. In systems with stronger long-range interactions, the balance between the trends is achieved with higher collision energy. Neon has a stronger long-range interaction with the Ar^+ ion than does helium owing to its higher polarizability [28]. Therefore, we expect an increased AI/PI branching ratio at low collision energy, and a higher collision energy at which the AI and PI reaction rates will intersect.

In order to show that the differences in the branching ratios between $\text{Ne}^* + \text{Ar}$ and $\text{He}^* + \text{Ar}$ originate from the different long-range interaction strengths at the region of interaction, we calculate the PI and AI reaction rates with fictitious C_4 values. Interestingly, the neutral potential, the decay rate (Γ), the reduced mass (μ), and the short-range part of the ionic potential remain unchanged. The energy at which the AI and PI rates are equal is presented in Figure 4 for every fictitious value of C_4 . In the two systems, we observe the same dependence of the energy at which the branching ratio equals unity on the value of C_4 , despite the differences in the unmodified parameters. This indicates that the different long-range interactions are indeed responsible for the significant differences in the branching ratios between the two systems.

Recently, Gordon et al. [29] measured the PI and AI reaction rates in the case of $\text{Ne}^* + \text{Ar}$ ionisation in the presence of external magnetic field. Their measurements clearly show that the branching ratio strongly depends on the relative orientation of the magnetic field and the collision axis. We demonstrate here that the same model that was used by the authors [29,30] does not reproduce the branching ratio control. The exact decay rates from the different magnetic projection states into each of the three final ionic spin-orbit states are not known and are

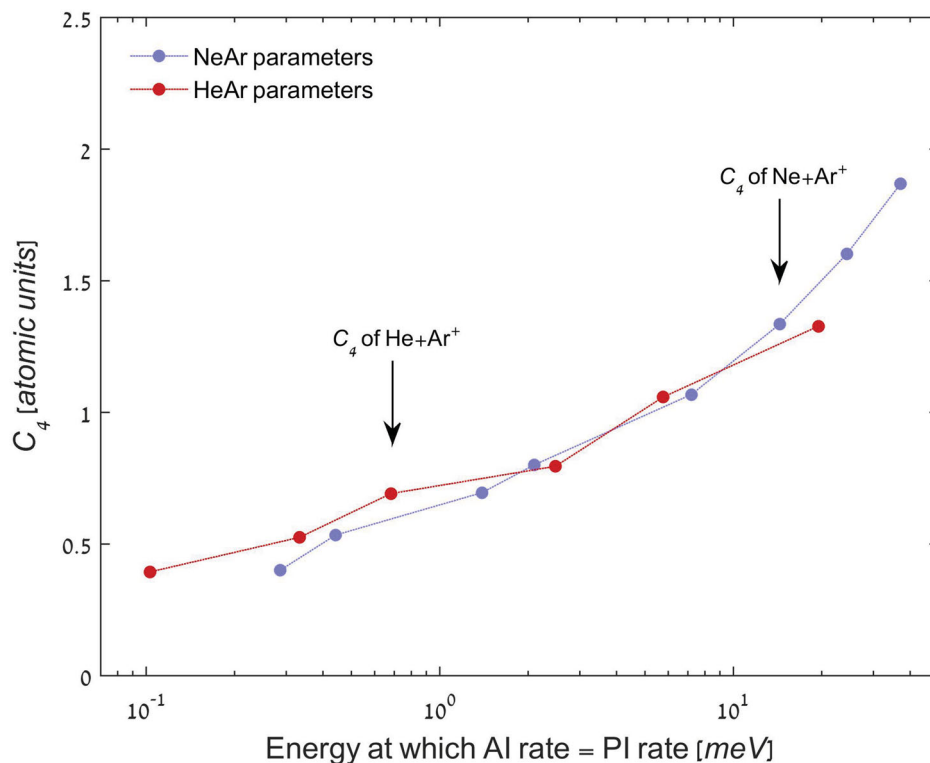


Figure 4. Semi-log plot of the calculated energy at which the AI and PI rates are equal versus a parametric variation of C_4 coefficients for $\text{Ne} + \text{Ar}^+$ (blue) and $\text{He} + \text{Ar}^+$ (red). The parameters V_{neutral} , Γ , μ and the short-range part of the ionic potential were not modified. The C_4 ion-induced dipole interaction coefficients of $\text{He} + \text{Ar}^+$ and $\text{Ne} + \text{Ar}^+$ (0.692 and 1.335 atomic units, respectively) are denoted by arrows. In these cases the value of C_4 , in atomic units, is equal to half of the electric polarizability of the atom [28] (colour online).

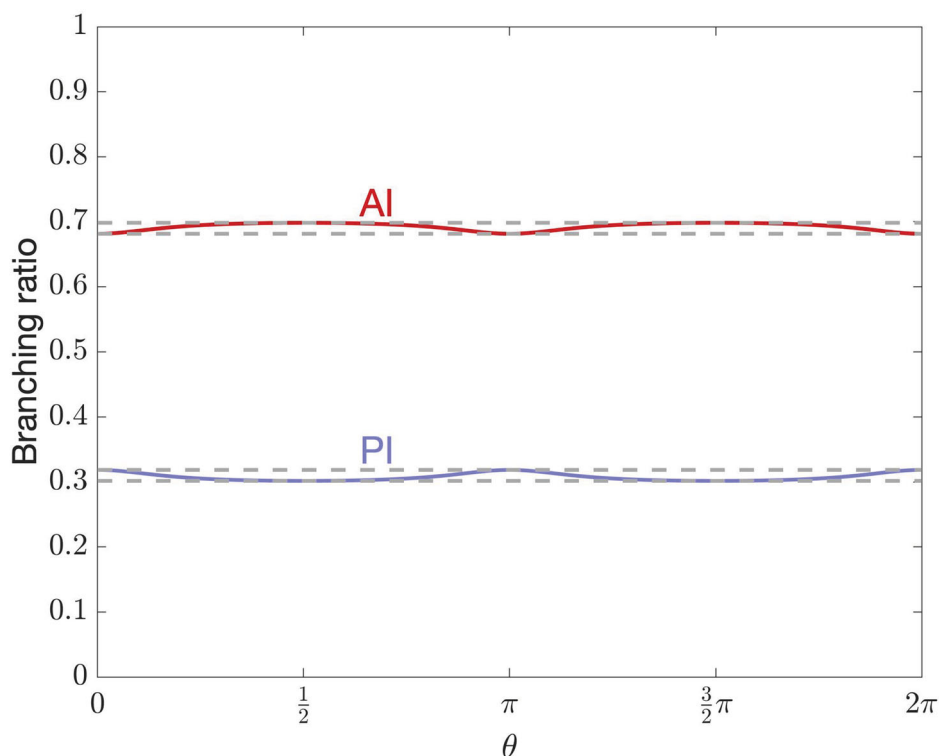


Figure 5. Calculated PI and AI ratios as a function of θ , the external magnetic field direction relative to the collisions axis, for the case of $\text{Ne}^* + \text{Ar}$. Dashed lines show the bounds for the scanned 10^7 sets of individual decay rates; continuous lines are PI and AI branching ratios for the case with the maximal change.

empirically taken to have an exponential form. Whereas the pre-exponential factor might vary, the exponential argument remains the same [14]. Therefore, we scan over many (10^7) sets of pre-exponential factors. We find that the maximal change in branching ratio as a function of the magnetic field orientation relative to the collision axis, does not exceed 10%. The simulation with the largest change in the AI and PI branching ratio, at a collision energy of 175 K, is presented in Figure 5.

Conclusion

In contrast to strongly interacting systems, where the branching ratio does not vary significantly as a function of the collision energy, weakly interacting systems exhibit major changes in the branching ratio over a wide range of collision energies. Our study indicates that in strongly interacting systems, where the potential well depth is larger compared to the reaction collision energies, the shape of the incoming wave functions in the region of reaction is determined mainly by the depth of the well. Therefore, different incoming wave functions have a relatively similar shape and similar overlaps with final states. In this case, the only expected dependence of the branching ratio on collision energy originates from populating high angular momentum states at higher collision energies. The high angular momentum states lack bound states due to the high centrifugal repulsion, and therefore contribute only to the continuum channel, i.e. PI. In contrast, in weakly interacting systems, the shape of the incoming wave functions in the region of reaction depends more sensitively on the collision energy, resulting in an energy-dependence of the branching ratio. In particular, we have measured significant changes in the branching ratio in van der Waals weakly interacting $\text{Ne}^* + \text{Ar}$ and $\text{He}^* + \text{Ar}$ with PI and AI product channels over a wide range of collision energies. At high collision energies, PI is the major channel in both systems. At low collision energy, AI is clearly dominant in the $\text{Ne}^* + \text{Ar}$ reaction, while being comparable to PI in $\text{He}^* + \text{Ar}$. The difference between the two systems is attributed to a stronger ion-induced dipole interaction, i.e. a larger C_4 value in $\text{Ne} + \text{Ar}^+$, which leads to faster oscillations and thus to lower overlaps of the continuum ionic wave functions with the weighted incoming reactant wave function.

In this work we have measured the dependence of the branching ratio on the collision energy in two weakly interacting systems. Our theoretical work explains why this dependence is weaker in systems with stronger interactions, and attributes the differences in branching ratios between the two weakly interacting systems to the product's potential details.

Disclosure statement

No potential conflict of interest was reported by the authors.

Funding

This work was supported by Israel Science Foundation: [Grant Number 1810/13]; The European Commission: [Grant Number EU-FP7-ERC-CoG 1485]; Alexander von Humboldt foundation.

ORCID

Natan Bibelnik  <https://orcid.org/0000-0002-0308-6319>

Wojciech Skomorowski  <http://orcid.org/0000-0002-0364-435X>

References

- [1] F.H.J. Hall and S. Willitsch, *Phys. Rev. Lett.* **109**, 233202 (2012).
- [2] W.G. Rellergert, S.T. Sullivan, S. Kotochigova, A. Petrov, K. Chen, S.J. Schowalter and E.R. Hudson, *Phys. Rev. Lett.* **107**, 243201 (2011).
- [3] L. Ratschbacher, C. Zipkes, C. Sias and M. Köhl, *Nat. Phys.* **8**, 649 (2012).
- [4] J. Deiglmayr, A. Göritz, T. Best, M. Weidemüller and R. Wester, *Phys. Rev. A* **86** (2012).
- [5] D. Gerlich and G. Borodi, *Faraday Discuss.* **142**, 57 (2009).
- [6] P. Allmendinger, J. Deiglmayr, K. Höveler, O. Schullian and F. Merkt, *J. Chem. Phys.* **145**, 244316 (2016).
- [7] A.B. Henson, S. Gersten, Y. Shagam, J. Narevicius, and E. Narevicius, *Science* **338**, 234 (2012).
- [8] B. Bertsche, J. Jankunas and A. Osterwalder, *Chim. Int. J. Chem.* **68**, 256 (2014).
- [9] E. Lavert-Ofir, Y. Shagam, A.B. Henson, S. Gersten, J. Klos, P.S. Żuchowski, J. Narevicius and E. Narevicius, *Nat. Chem.* **6**, 332 (2014).
- [10] A. Klein, Y. Shagam, W. Skomorowski, P.S. Żuchowski, M. Pawlak, L.M.C. Janssen, N. Moiseyev, S.Y.T. van de Meerakker, A. van der Avoird, C.P. Koch and E. Narevicius, *Nat. Phys.* **13**, 35 (2016).
- [11] Y. Shagam, A. Klein, W. Skomorowski, R. Yun, V. Averbukh, C.P. Koch, and E. Narevicius, *Nat. Chem.* **7**, 921 (2015).
- [12] J. Jankunas, B. Bertsche, K. Jachymski, M. Hapka and A. Osterwalder, *J. Chem. Phys.* **140**, 244302 (2014).
- [13] J. Jankunas, B. Bertsche and A. Osterwalder, *J. Phys. Chem. A* **118**, 3875 (2014).
- [14] P.E. Siska, *Rev. Mod. Phys.* **65**, 337 (1993).
- [15] W.H. Miller, *J. Chem. Phys.* **52**, 3563 (1970).
- [16] K. Luria, N. Lavie and U. Even, *Rev. Sci. Instrum.* **80**, 104102 (2009).
- [17] U. Even, J. Jortner, D. Noy, N. Lavie and C. Cossart-Magos, *J. Chem. Phys.* **112**, 8068 (2000).
- [18] Y. Shagam and E. Narevicius, *J. Phys. Chem. C* **117**, 22454 (2013).
- [19] D.T. Colbert and W.H. Miller, *J. Chem. Phys.* **96**, 1982 (1992).
- [20] B.R. Johnson, *J. Chem. Phys.* **67**, 4086 (1999).
- [21] A.P. Hickman, *J. Phys. B At. Mol. Phys.* **9**, 1765 (1976).
- [22] H. Morgner, *J. Phys. B At. Mol. Phys.* **11**, 269 (1978).

- [23] P.E. Siska, *Chem. Phys. Lett.* **63**, 25 (1979).
- [24] R.W. Gregor and P.E. Siska, *J. Chem. Phys.* **74**, 1078 (1981).
- [25] T.P. Parr, D.M. Parr and R.M. Martin, *J. Chem. Phys.* **76**, 316 (1982).
- [26] A. Blech, Y. Shagam, N. Hölsch, P. Paliwal, W. Skomorowski, J.W. Rosenberg, N. Bibelnik, O. Heber, D.M. Reich, E. Narevicius and C. Koch, Phase protection of Fano-Feshbach resonances (submitted). arXiv:1902.09262.
- [27] H.J. Werner, P.J. Knowles, R. Lindh, F.R. M. M. Schütz, P. Celani, T. Korona, A. Mitrushenkov, G. Rauhut, MOLPRO, version 2010.1, a package of ab initio programs. See <http://www.molpro.net>. (2010).
- [28] T.M. Miller, *Adv. At. Mol. Phys.* **13**, 1 (1978).
- [29] S.D.S. Gordon, J.J. Omiste, J. Zou, S. Taneri, P. Brumer and A. Osterwalder, *Nat. Chem.* **10**, 1190 (2018).
- [30] S.D.S. Gordon, J. Zou, S. Taneri, J. Jankunas and A. Osterwalder, *Phys. Rev. Lett.* **119**, 053001 (2017).